Large Scale 3D Flow Distribution Analysis in HTPEM Fuel Cells

C. Siegel[*1,2], G. Bandlamudi[1,2], N. van der Schoot[1] and A. Heinzel[1,2]

[1]Zentrum für BrennstoffzellenTechnik (ZBT) GmbH, Duisburg, Germany

[2]University of Duisburg-Essen, Institut für Energie- und Umweltverfahrenstechnik, Duisburg, Germany

*Corresponding author: Zentrum für BrennstoffzellenTechnik (ZBT) GmbH, Carl-Benz-Straße 201, D-47057 Duisburg, Germany, c.siegel@zbt-duisburg.de

Abstract: Accurate bipolar-plate and flow-field layout is one crucial task for optimizing fuel cells. These cell components perform several functions, including charge transport or gas and water transport throughout the cell just to name a few. Overall, the design depends on the fuel cell application or the geometrical size of the assembly. The requirements for a flow-field used in a high temperature polymer electrolyte membrane (HTPEM) fuel cell (operated at temperatures around 130-180°C) differ from the ones that are important in the field of low temperature polymer electrolyte membrane (LTPEM) fuel cells, mainly operated around 80°C. In a HTPEM fuel cell, liquid product water is not present during operation, thus porous media flooding is less of a concern. Nevertheless, large quantities gradients should be avoided. Uniform fluid-flow is of utmost importance.

Keywords: High temperature PEM (HTPEM) fuel cell, flow-field, bipolar-plate, PIV measurement, fluid-flow.

1. Introduction

HTPEM fuel cells are receiving increased attention in the past years. They are suitable energy converters for many applications such as backup power units or automotive applications. Nevertheless, much work needs to be done in order to optimize these cells and to ensure proper gas supply to the reaction sights. In terms of fluid-flow, one must consider the application requirements (e.g. gas composition) and the layout of the complete cell itself. It is known that the electrochemical half-cell reactions depend on e.g. the mass/mole fraction of the species, thus they depend on the fluid-flow and the flow-field type. A good review about flow-field design can be found in e.g. [1].

This work is based on the previous HTPEM fuel cell models developed by our group [2,3] and highlights the fluid-flow in large scale flow-fields. A 50 [cm^2] six channel parallel serpentine flow-field is used as a reference. The computed results of the reference case are compared to data obtained by particle image velocimetry (PIV) performed at our institute. Six different flow-field types are presented and discussed, keeping the active area, the channel to land ratio, and the position of the gas in-, and outlets constant:

- Parallel serpentine (2x)
- Mixed (2x)
- Straight
- Criss-cross (a.k.a. pin hole)

The aim of this contribution is to compare the fluid-flow behaviour in terms of e.g. pressure loss, maximum velocity, average velocity, or gas bypassing between adjacent channels. Note that in HTPEM fuel cells, water removal is less of a concern since no liquid water is present during operation. Nevertheless, it must be noted that condensed water along with (excess) phosphoric acid may be present during start-up and shut down periods.

2. Governing Equations and Analytical Calculations

2.1 Transport Equations

COMSOL Multiphysics v3.5a was used along with analytical calculations in order to investigate the cathode side velocity and pressure distribution (momentum transport).

$$\nabla \cdot u = 0$$
$$\rho \cdot u \cdot \nabla u =$$
$$\nabla \cdot \left(-P \cdot I + \eta \cdot \left(\nabla u + (\nabla u)^T \right) \right) \quad (1)$$
$$+ F$$

The fluid-flow within the gas channels was modeled with the incompressible Navier-Stokes application mode (laminar flow) (1).

For the fluid-flow through the porous media, the software offers the possibility of using i) the Brinkman equations (2)

$$\nabla \cdot u = 0$$

$$\frac{\eta}{k_p} \cdot u =$$

$$\nabla \cdot \left(-P \cdot I + \frac{1}{\varepsilon} \cdot \left(\eta \cdot \left(\nabla u + (\nabla u)^T \right) - \frac{2}{3} \cdot \eta \cdot (\nabla u) \cdot I \right) \right) + F \qquad (2)$$

or ii) Darcy's law equation (3) which is a subset of the Brinkman equations.

$$u = -\frac{k_p}{\eta} \cdot \nabla P \qquad (3)$$

The velocity results from the pressure gradient in the porous media. In the above equations, u is the velocity [m·s^{-1}], P the pressure [Pa], ρ is the density [kg·m^{-3}], η the dynamic viscosity [Pa·s^{-1}], k_p the permeability of the porous media [m^2], and ε the porosity of the porous media [-]. F represents the body force vector [N·m^{-3}].

The Brinkman equations can be used for slightly faster porous media flows whereas the Darcy's law equation is often used for slow porous media flow. Generally, one has to study the terms within the equations to determine which is the most appropriate for a particular application. The physical properties of air were directly taken from the software.

2.2 Boundary and Initial Conditions

The same laminar inflow condition was used for all computations (adding an additional weak contribution – pressure variable *Pinl_chns*). At the outlet, a pressure condition was applied (no backpressure). The default no slip boundary condition was used for all gas channel walls. When using the Brinkman equations along with the Navier-Stokes equations, note that at the gas channel to porous media interface continuity is automatically used. However, when using the Darcy's law equation for porous media flow, one has to work with a set of constraints on pressure and velocity at this interface.

The above equations are very sensitive to the initial guess. Good values can iteratively be achieved by using a series of dummy simulations.

2.2 Analytical Calculations

Simple analytical calculations were used in order to guess and/or cross-check the results. Setting an initial guess is easier by knowing the order of magnitude for different variables. Typical equations can be found in e.g. [4]. The pressure loss between the inlet and outlet is proportional to the flow rate.

$$\Delta P = f \cdot \frac{l_{ch}}{D_H} \cdot \rho \cdot \frac{\bar{u}^2}{2} + \sum K_l \cdot \rho \cdot \frac{\bar{u}^2}{2} \qquad (4)$$

In equation (4), f is a friction coefficient [-], l_{ch} the channel length [m], and K_l the local resistance in sharp turns. The hydraulic diameter is calculated using equation (5)

$$D_H = \frac{4 \cdot a_{ch}}{p_{ch}} \qquad (5)$$

In the above equation a_{ch} is the cross-sectional area [m^2] and p_{ch} the channel perimeter [m]. The channel length can be approximated with

$$l_{ch} = \frac{a_{MEA}}{n_{ch} \cdot (w_{ch} + w_l)} \qquad (6)$$

In equation (6), a_{MEA} is the active are of the cell [m^2], n_{ch} the number of parallel channels [-], and w the width of the channel and land respectively [m].

For a laminar flow in a rectangular gas channel, the product of the Reynold's number and the friction factor is defined by Re $\cdot f = 56$. The local resistance can be approximated with $30 \cdot f$ for 90° bends and $50 \cdot f$ for close return bends.

Laminar flow conditions in the gas channels can quickly be checked using equation (7).

$$\mathrm{Re} = \frac{\rho \cdot \bar{u} \cdot D_H}{\eta} \qquad (7)$$

Finally, the mean velocity within a gas channel is calculated using the total volume flow rate v_{cell} [$m^3 \cdot s^{-1}$].

$$\bar{u} = \frac{v_{cell}}{n_{ch} \cdot a_{ch}} \qquad (8)$$

3. Modeling Geometry – Gas Channel and Porous Media

Elaborated tests at the ZBT laboratory showed that in a HTPEM fuel cell optimal fluid-flow is more important on the cathode side than on the anode side. Oxygen has to partially diffuse into the H_3PO_4 to reach the reaction sights. The reference case modeling geometry is given in Fig.1.
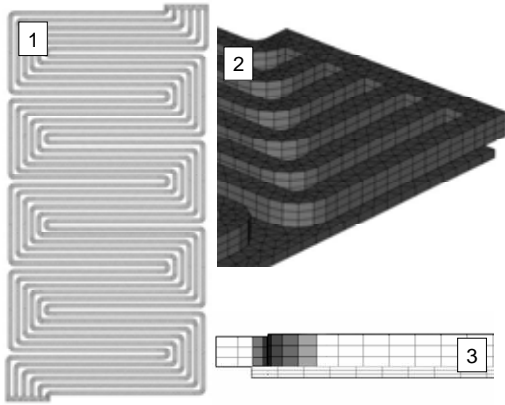

Figure 1. 50 [cm^2] six channel parallel serpentine flow-field (cathode side). Top view (x-y-plane) (1); in-, outlet section (2); side view (z-x-plane) (3).

The porous media subdomain was treated as a woven-type gas diffusion layer (GDL), similar to E-tek - ELAT® products. The uncompressed thickness l_0 was roughly 400 [µm] with an assumed porosity of 0.69 [-], and a permeability of $2 \cdot 10^{-12}$ [m^2]. For the GDL areas that are in direct contact with the bipolar-plate (i.e. land area), a maximum compression of 20% was assumed. The following equation was used to correlate the porosity values for a GDL thickness l.

$$\varepsilon = \frac{l_0}{l} \cdot (\varepsilon_0 - 1) + 1 \qquad (4)$$

This model offers the possibility to account for different material properties at different locations depending on the flow-field type.

The following table summarizes the geometrical aspects, including the channel to land ratio ([mm]) and the channel to land contact area ratio ([%]) at the porous media interface.

Table 1: Geometrical aspects.

Type	Channel/land	Contact area
Serpentine 1	1/1	52.3/47.7
Serpentine 2	1/0.9	52.6/47.4
Mixed 1	1/1	50.6/49.4
Mixed 2	1/1	54.1/45.9
Straight	1/1	50.7/49.3
Criss-cross	n.a.	73.5/26.5

4. Meshing and Solver Settings

A swept free mesh (prism elements) was used for all geometries. The maximum element size was set to $0.85\text{-}1 \cdot 10^{-3}$ [-]. The following table summarizes meshing details and the resulting number of degrees of freedom (DOF).

Table 2: Meshing details.

Type	Mesh elements	DOF
Serpentine 1	137,898	2,075,382
Serpentine 2	126,972	1,914,108
Mixed 1	121,233	1,829,532
Mixed 2	121,257	1,828,349
Straight	113,187	1,705,113
Criss-cross	58,988	1,055,744

Since a large amount of RAM was available, a parallel sparse direct linear solver (PARDISO) was used whenever possible. In most cases, however, an iterative solver was used (BiGCStab (linear system solver) – GM (3 level preconditioner) – Vanka (presmoother with pressure update) – Vanka (postsmoother with pressure update) – PARDISO (coarse direct solver). The relative tolerance was set to $1 \cdot 10^{-4} - 1 \cdot 10^{-6}$.

Better convergence behaviour was observed when using the Navier-Stokes/Brinkman equations instead of the Navier-Stokes/Darcy's law equation. This can be explains by the fact of

the slight incompatibility of both equation forms (5 dependent variables against 1 dependent variable). It is recommended to add non-ideal weak constraints to the equation system (Lagrange multipliers (*lm*) are added that equalize the DOF of the two equation systems) [5]. Additionally, a parametric solver was used in order to gradually de-, or increase the viscosity and/or inlet condition.

5. Results

5.1 PIV Measurements

Experimental fluid-flow data was obtained by particle image velocimetry (PIV) performed at our institute (Fig.2) [6]. The experimental set-up consisted of a 12-bit CCD camera with a high resolution, a fluorescence filter, a dual-pulse Nd:YAG (neodymium-doped yttrium aluminum garnet) laser, and a software.
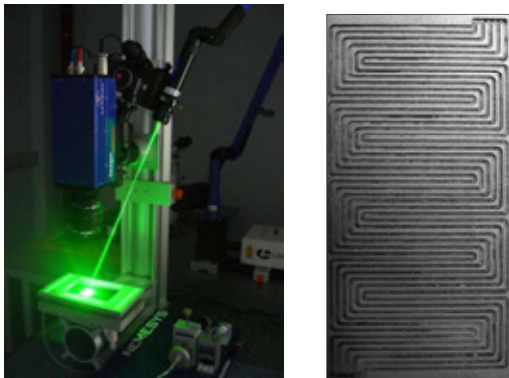

Figure 2. Reference case PIV measurements using a transparent cell (left); in-house developed six channel parallel serpentine flow-field (right) [7].

The basic principle of PIV is that two laser-illuminated images of the seeded flow are acquired at successive time instants, separated by Δt. The 50 [µm] polystyrene seed particles, fluoresce stimulated by the volume illumination of the laser, appear as bright spots in the digital image. The measurement plane is defined by depth of focus of the Objective.

Each image is broken down into a series of interrogation windows. For each interrogation window, the intensity of the signal within the

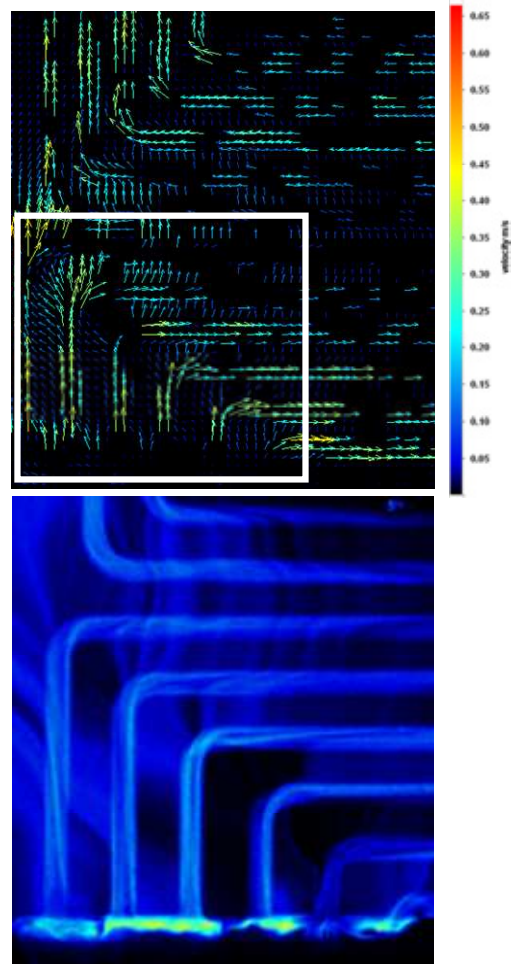window is cross-correlated between image 1(*t*) and image 2(*t*+Δt).

Figure 3. Detailed view of the measured water velocity (min to max: 0 to 0.65 [m·s^{-1}]) close to the gas channel inlet section (top); zoom on the gas bypassing between adjacent channels (bottom).

The cross-correlation peak within this window corresponds to an average displacement of the seed particles, and when divided by Δt, provides an average velocity for the particles within this interrogation window. Velocity fields can instantaneously be measured with a high spatial resolution by cross-correlating the full series of interrogation windows within an image pair.

A dimensional analysis using the Reynold's number was performed since the PIV

measurements were realized in water model conditions. Doing so ensured dynamic similarity to a gas inlet flow-rate of 1 [l·min^{-1}] air.

In Fig.3 it is seen how the fluid-flow mainly follows the six parallel serpentine channels. The measured pressure loss over the flow-field was 22-25 [mbar]. Slightly higher velocity values were observed in the middle of each gas channel. Gas bypassing between adjacent channels was seen in the regions of highest pressure difference (gas flows from an upstream leg of a channel to a downstream leg of the same channel though the porous media under the land of the bipolar-plate).

5.2 Simulated Results

Fig.4 shows the simulated velocity within the porous media and the pressure loss (reference case).
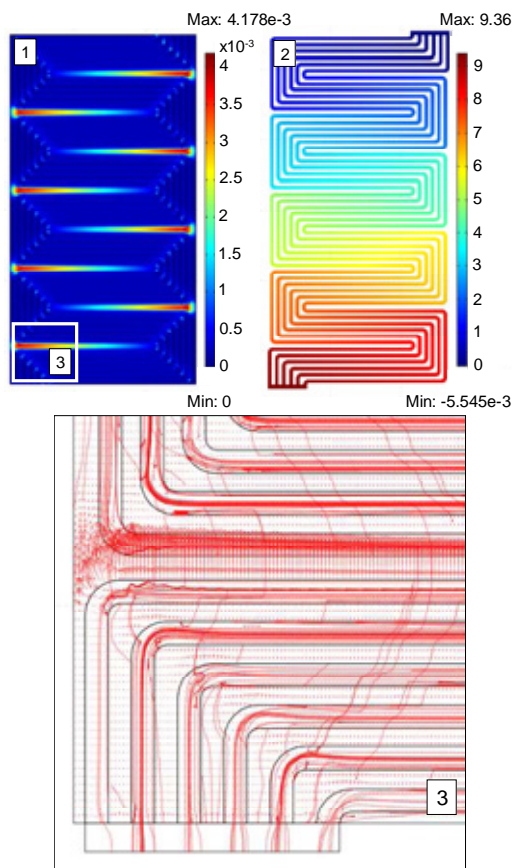

Figure 4. Velocity within the porous media (slice plot) (1); pressure loss (slice plot) (2); zoom of the inlet section highlighting the velocity vectors and the velocity streamlines (3).

The influence of the flow-field type on the porous media flow can clearly be seen. Higher lateral velocities (up to 9·10^{-3} [m·s^{-1}]) are observed in the regions under the gas channel bends and especially in the regions of the highest pressure difference. The gas bypassing between adjacent channels shows the same trend as in Fig.3. The maximum velocity is 5.832 [m·s^{-1}], located within the middle of the gas channels (z = 500·10^{-6} [m]). The pressure loss was simulated to be around 10 [mbar] whereas the analytically calculated values returned 11-13 [mbar].

Fig.5 displays the velocity within the porous media and within the middle of the gas channels for the serpentine 2 type flow-field (nine channels parallel). In the porous media, highest values are observed close to the regions of the highest pressure difference. The maximum velocity is 5.631 [m·s^{-1}], located close to the in,- and outlet. The pressure loss was 4.5 [mbar].
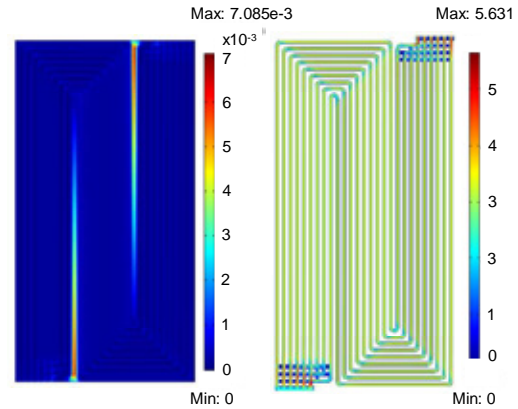

Figure 5. Velocity within the porous media (slice plot) (left); velocity within the gas channels (slice plot) (right).

The obtained results for the mixed type flow-fields are given below. They consist of six main gas channels, each of them divided into a number of straight (parallel) gas channels. The mean velocities are slightly lower when comparing them to both serpentine flow-fields. Consequently, only a low pressure loss occurs. The maximum velocity of 6.054 [m·s^{-1}] (mixed

1) and 5.738 [m·s⁻¹] (mixed 2) is located in the main channels. Both topologies returned a quite uniform flow distribution in their straight (parallel) gas channel segments (i.e. central region of the active area).
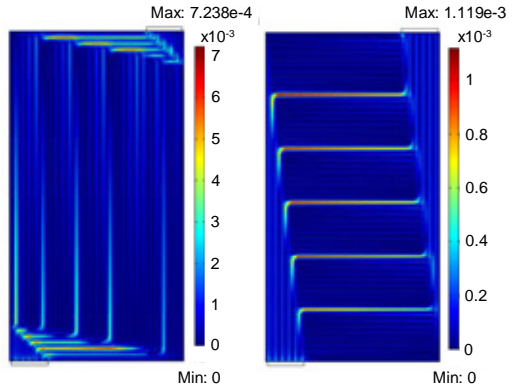

Figure 6. Mixed 1 type flow-field velocity within the porous media (slice plot) (left); mixed 2 type flow-field velocity within the porous media (slice plot) (right).

The simulated results for the straight flow-field are depicted in Fig.7. The position of the in-, and outlet forces the fluid to flow preferable to the outer channels, whereas the velocity in the central region is almost stagnant.
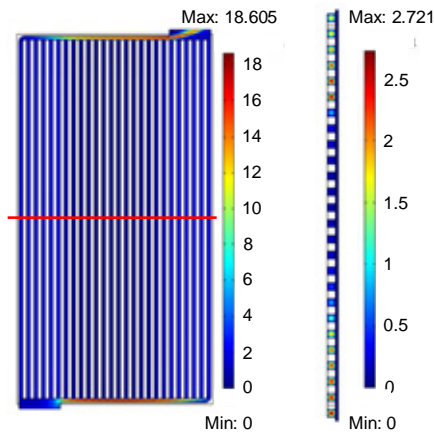

Figure 7. Gas channel velocity (left) (slice plot – x-y-plane); gas channel and porous media velocity (slice plot along the red line – y-z-plane) (right).

The overall maximum velocity values are predicted in the single channel that connects all straight channels (18.6 [m·s⁻¹]).

Fig.8 highlights the above discussed aspects. It shows the absolute velocity along the y-axis (z = 500·10⁻⁶ [m]). The influence of the in-, and outlet on the flow distribution is clearly visible.
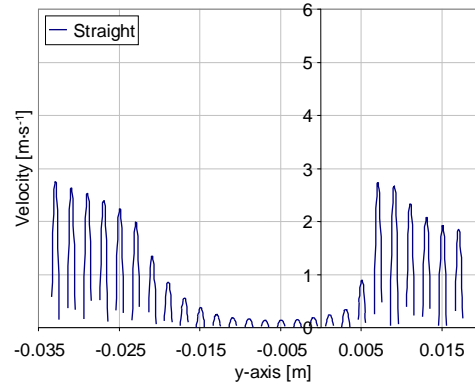

Figure 8. Gas channel velocity (absolute values along the y-axis – see red line in Fig.7).

The criss-cross type flow-field consisted of transversal and longitudinal channels forming an array of squared pins. The maximum velocity is 2.168 [m·s⁻¹], whereas lowest velocity values are observed in the top left and lower right corner. Overall, the flow distribution is relatively uniform over the MEA area but depended on the positioning of the in-, and outlet (see streamline plot).
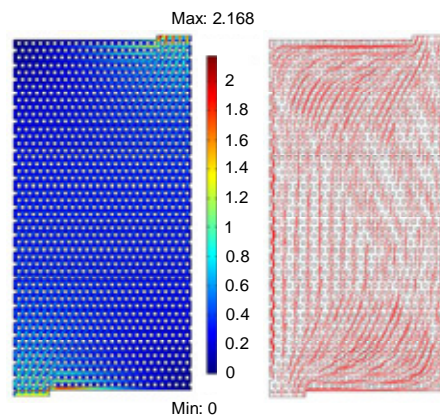

Figure 9. Gas channel velocity (left) (slice plot – x-y-plane); gas channel streamline plot (right).

Table 3 summarizes the simulated results for the gas channels and the porous media flow. The highest velocity values were observed in the

serpentine 1 type flow-field (highest pressure loss), followed by the serpentine 2 type. The straight type flow-field showed third highest values. The criss-cross type flow-field returned the lowest overall values. A relatively high porous media velocity was seen for the straight type flow-field when comparing it to its low gas channel velocity of 0.849 [m·s^{-1}]. Moreover it must be noted that the porous media velocity for both mixed type flow-fields was significantly lower than for other types.

Table 3: Simulated fluid-flow data (mean values).

Type	u_{ch}	u_{GDL}	ΔP	Re
Serpentine 1	2.667	4.66e-4	9.36	72.3
Serpentine 2	1.778	2.88e-4	4.5	46.8
Mixed 1	0.866	8.79e-5	1.48	21.1
Mixed 2	0.799	9.67e-5	1.88	23.9
Straight	0.849	2.75e-4	3.58	23.7
Criss-cross	0.232	n.a.	0.4	15.4

7. Conclusions

Different types of flow-fields were modeled and simulated using COMSOL Multiphysics in order to highlight their fluid dynamics performance. The reference case was compared to PIV measurements and a good agreement was found. Quantitatively, similar fluid-flow behaviour was observed, showing that both tools can be used in future for design and layout purpose. Moreover, the analytically calculated results matched the simulated results, whereas the measured pressure loss was slightly higher than the simulated one. As for the fluid-flow, a quite homogeneous velocity and pressure field was found for both serpentine flow-fields. The same argument holds for the criss-cross type flow-field, whereas the straight type flow-field yields an inherent maldistribution. Based on the achieved results, one cannot make a final statement as flow-field design and layout includes more than momentum transport. For HTPEM fuel cells, it seems evident that one possibility to substantially improve flow-fields is to modify the position of the (multiple) in-, and outlet(s) or to design a gas distributor before entering the active area. This will probably lead to more uniform quantities distribution. Additionally, the gas bypassing between adjacent channels (lateral flow) should be evaluated for HTPEM fuel cells in terms of e.g. local current densities distribution. So, reactant utilization needs to be interpreted differently as it is the case for LTPEM fuel cells as liquid water is not present during operation nor it is explicitly needed for proton transport.

8. References

1. Li, X., Sabir, I., Review of bipolar plates in PEM fuel cells: Flow-field designs, *Int. J. Hydrogen Energy*, **30**, 359-371 (2005)
2. Siegel, C., Bandlamudi G., Heinzel, A., *Numerical simulation of a high-temperature PEM (HTPEM) fuel cell*, Oral presentation, Published in: Proceedings of the European COMSOL Conference, Grenoble, France (2007)
3. Siegel, C., Bandlamudi, G., Heinzel, A., *Modeling polybenzimidazole/phosphoric acid membrane behaviour in a HTPEM fuel cell*, Oral presentation, Published in: Proceedings of the European COMSOL Conference, Hannover, Germany (2008)
4. Spiegel, C., *PEM fuel cell modeling and simulation using MATLAB®*, Academic Press, London (2008)
5. COMSOL Multiphysics (2009)
6. van der Schoot, N., Lindken, R., Sharp, K.V. Peil, S., Wartmann, J., Westerweel, J., *PIV-measurements for investigation in fuel cells*, Fachtagung 'Lasermethoden in der Strömungsmesstechnik', Karlsruhe, Germany (2008)
7. Derieth, T., Bandlamudi, G., Beckhaus, P., Kreuz, C., Mahlendorf, F., Heinzel, A., Development of highly filled graphite compounds as bipolar plate materials for low and high temperature PEM fuel cells, *J. New Mat. Electrochem. Systems,* **11,** 21–29 (2008)

9. Acknowledgements